Assessment of Gas-Fluidized Beds Mixing and Hydrodynamics by Zirconia Sensors

Roberto Solimene, Antonio Marzocchella, Gabriella Passarelli, and Piero Salatino
Dipartimento di Ingegneria Chimica - Università degli Studi di Napoli Federico II, Istituto di Ricerche sulla Combustione CNR, P.le V. Tecchio 80, 80125 Napoli, Italy

DOI 10.1002/aic.10592
Published online September 23, 2005 in Wiley InterScience (www.interscience.wiley.com).

Gas-mixing and bed hydrodynamics associated with the rise of isolated bubbles in gas-fluidized beds of two granular solids are investigated by means of a novel technique. These diagnostics consist of an array of miniaturized zirconia-based oxygen sensors located along the axis of a hot (1123 K) incipiently fluidized bed, in which isolated bubbles of a tracer gas (nitrogen) are injected. Time-resolved oxygen concentrations and relative pressures are recorded at several levels along the bed. It is shown how the response of the sensors array can be related to the concurrent effects of bubble motion, bubble-emulsion phase, mass transfer and interstitial gas flow in the emulsion phase, combined with each other to give rise to the propagation of two perturbations to the basal value of oxygen concentration. Analysis of time-resolved oxygen concentration profiles enables the assessment of: (a) the bubble rise velocity; (b) the gas velocity associated with the interstitial flow; and (c) the interphase bubble-emulsion phase, mass-transfer rate and coefficient. Analysis of the response of sensors located in the splash zone of the fluidization column provides indirect inference of the hydrodynamic patterns associated with bubble bursting at the surface of the bed. © 2005 American Institute of Chemical Engineers *AIChE J,* 52: 185-198, 2006

Keywords: gas-solid fluidization, mixing, hydrodynamics, bubbles, mass-transfer coefficient, zirconium oxide sensors

Introduction

The relevance of mass transfer between bubbles and the emulsion phase to the effectiveness of a broad range of fluidized bed, chemical and physical processes, has long been highlighted. Several examples can be provided: (a) char burnout in bubbling fluidized-bed combustors (or in the bottom bed of circulating FBC), where heterogeneous char combustion is fast to the point of making interphase mass transfer the rate-controlling process; (b) burning of combustible gas in bubbling fluidized beds, where homogeneous reaction is quenched in the emulsion phase, whereas it takes place in the bubbles at a rate that can be controlled by mass transfer; and (c) fast catalytic reactions, like the catalytic combustion of light hydrocarbons. Despite the recognition of the role of interphase mass transfer in a variety of fluidized bed processes, and the extensive literature published on this topic,[1-9] there is still a lack of experimental data and phenomenological modeling related to this subject.

Mass transfer between a bubble and the emulsion phase is typically described by the following balance on species A

$$-\frac{dN_{Ab}}{dt}\frac{1}{V_b} = K_{be}(C_{Ab} - C_{Ae}) \tag{1}$$

where N_{Ab}, V_b are the number of moles of A in the bubble and the bubble volume K_{be} is the overall bubble-to-emulsion phase mass-transfer coefficient per unit volume of the bubble, and C_{Ab} and C_{Ae} are the concentrations of A in the bubble and in the

Correspondence concerning this article should be addressed to P. Salatino at salatino@unina.it.

emulsion phase, respectively. In the case of fast bubbles (rising bubble velocity larger than interstitial gas velocity), characterized by the presence of a gas cloud, the overall mass-transfer coefficient between the emulsion phase, and the bubble phase per unit volume of the bubble is determined as the sum of two resistances in series: (1) mass transfer from the bubble to the cloud K_{bc}; (2) mass transfer from the cloud to the bulk of the emulsion phase K_{ce}. Accordingly

$$K_{be} = \frac{1}{\frac{1}{K_{bc}} + \frac{1}{K_{ce}}} \tag{2}$$

Several models have been published for the prediction of the overall mass-transfer coefficient between a single bubble and the emulsion phase. They are generally based on the consideration of the hydrodynamics associated with the motion of an isolated bubble rising along the fluidized bed and of the flow patterns in the emulsion phase around the bubble.

Davidson and Harrison[10] developed a mass transfer model between a single bubble and the emulsion phase, based on Davidson's analysis of bubble motion, valid for clouded bubbles. They assumed that gas composition inside the cloud coincides with that of the emulsion phase. Accordingly, the overall mass-transfer coefficient can be estimated considering the resistance to mass transfer between the bubble and the cloud. It is

$$K_{be} = K_{bc} = 4.5\left(\frac{U_{mf}}{D_b}\right) + 5.85\left[\frac{(D)^{1/2}(g)^{1/4}}{(D_b)^{5/4}}\right] \tag{3}$$

where U_{mf}, D_b, D, and g are the minimum fluidization velocity, the bubble dia., the molecular gas diffusivity, and the acceleration due to gravity, respectively.

Kunii and Levenspiel[11] reconsidered the Harrison and Davidson model considering both the bubble-to-cloud and the cloud-to-emulsion phase mass-transfer rates. The Davidson and Harrison model was used to express the mass-transfer coefficient between the cloud and the bubble per unit volume of the bubble K_{bc}. The mass-transfer coefficient between the cloud and the emulsion phase per unit volume of the bubble was calculated according to the penetration theory of Higbie[12]

$$K_{ce} = 6.77\left(\frac{D\varepsilon_{mf}0.711\sqrt{gD_b}}{D_b^3}\right) \tag{4}$$

where ε_{mf} is the voidage at the incipient fluidization.

K_{be} was obtained by combining K_{ce} and K_{bc} according to Eq 2.

Chiba and Kobayashi[13] assumed that the controlling step to mass transfer between the bubble and the emulsion phase is associated with diffusion in the boundary layer between the cloud and the emulsion phase. Borrowing the streamline maps from the Murray[14] model, the authors expressed the overall mass-transfer coefficient between the bubble and the emulsion phase per unit volume of the bubble as

$$K_{be} = K_{ce} = \frac{6.78}{1 - f_w}\left(\frac{D\varepsilon_{mf}^2 U_b}{D_b^3}\right)^{1/2} \tag{5}$$

where f_w is the volumetric fraction of the wake behind the bubble and U_b the bubble rise velocity.

Sit and Grace[15] analyzed a large body of experimental results obtained in two-dimensional (2-D) fluidized beds for isolated bubbles and suggested a correlation for a 3-D single bubble, again based on Murray's analysis of bubble motion

$$K_{be} = 1.5\left(\frac{U_{mf}}{D_b}\right) + 5.71\left[\frac{(D)^{1/2}(g)^{1/4}}{(D_b)^{5/4}}\right] \tag{6}$$

In the case of slow bubbles ($U_b < \mathrm{Umf}/\varepsilon_{\mathrm{mf}}$), characterized by the short-cut of interstitial gas through the bubble, the overall mass-transfer coefficient between the emulsion phase, and the bubble phase per unit volume of the bubble is typically dominated by the convective term. Accordingly:

$$K_{be} = 1.5 \cdot k_{th} \cdot \frac{U_{mf}}{D_b} \tag{7}$$

where k_{th} depends on the bubble model used to represent the flow field around the bubble (for example, $k_{th} = 3$ for Davidson's model).

A major contribution to the collection of experimental data on interphase mass transfer in bubbling-fluidized beds has been given by professor Grace and coworkers.[15-17] The experimental procedure consisted of following the mixing process of tracer gas injected in a single bubble in a 2-D fluidized bed by means of a light absorption technique. Along a different path, Lignola et al.[18] developed a diagnostic setup for time- and space-resolved monitoring of gas composition in both the bubble and the particulate phases, based on quadrupole mass spectrometry. Also in this case, 2-D fluidized beds were used. The results were compared with predictions of Davidson's and Murray's models of bubble rise. An inherent difficulty arises when noninvasive techniques are applied to 3-D fluidized beds. On the other hand, techniques based on *in situ* gas sampling inevitably bring about some degree of intrusiveness and uncertainty. This drawback was partly overcome by the conditional gas sampling technique developed by Naruse et al.,[19] who measured only the concentration of the bubble phase by synchronizing gas sampling with the passage of the bubble. The latter was detected by pointwise measurement of differential pressure.

Gas-mixing in the splash zone of bubbling fluidized beds has received comparatively less attention, even if it plays a key role in the course of homogeneous chemical reactions in the splash zone and in the upper riser of bubbling/circulating fluidized beds. The performance and operational issues of processes like high-volatile fuel combustion/gasification are critically dependent on mixing/segregation of fuel-rich and fuel-lean gas streams.[20-22] It has been highlighted how gas mixing is related to the establishment of complex flow structures associated with bubble bursting at the bed surface. Different hydrodynamic models have been developed to describe such structures: the pioneering ghost bubble concept[23] and the intermittent jet model[24,25] have been recently reconsidered in the light of additional experimental investigations.[26-29] Altogether, the assessment of gas mixing downstream the dense bed is far less mature than

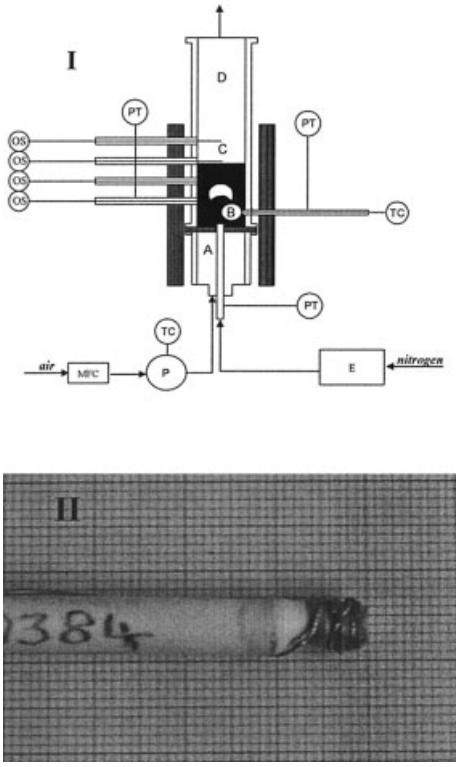

Figure 1. Experimental apparatus.

I. The fluidized bed plant: A wind-box; B fluidized bed; C splash zone; D freeboard; E bubble injector; P preheater. MFC: mass flow controllers. OS: solid state oxygen sensor. PT: pressure transducer. TC: thermocouple.

II. Tip of the zirconium oxide probe.

in-bed interphase mass transfer and calls for additional investigation.

This work aims at investigating gas-mixing phenomena associated with the rise of a single bubble in an incipiently gas fluidized bed. A novel experimental technique is envisaged, based on the measurement of time- and space-resolved oxygen concentrations by means of stabilized zirconia-based sensors. The main focus is represented by the assessment of the bubble-to-emulsion phase mass transfer, although a few tests were also directed to the assessment of the mixing pattern in the splash zone. Time- and space-resolved experimental data may prove useful for CFD models validation.

Experimental

Experimental apparatus

The experimental apparatus, represented in Figure 1:I, consisted of a cylindrical fluidization column equipped with a single bubble injection device, a set of pressure transducers, a set of solid state oxygen sensors, a set of thermocouples, and a data acquisition unit. The reactor consisted of a stainless-steel tube 0.102 m ID and 2 m high. The fluidization column was operated at atmospheric pressure and at temperatures up to 1123 K. The vessel was equipped with a low-pressure-drop distributor made of several stainless steel nets (mesh size of 50 μm) one on the other. The windbox was packed with ceramic rings to enhance gas preheating. The gas distributor and the windbox packing were effective in promoting uniform feeding of fluidizing gas.

The vessel was equipped with five tubes mounted flush to the column wall and located at distances from the distributor plate equal to $z = 0.04, 0.09, 0.14, 0.19, 0.24$ m. A thermocouple was fitted into the tube located at $z = 0.04$ m. Miniaturized oxygen sensors were fitted into the other tubes. Pressure taps were also located along the vessel at distances from the distributor equal to $z = 0.01, 0.04$ and 0.09 m. In particular, one pressure tap was located in the bubble injector tube ($z = 0.01$ m), one in the thermocouple fitting tube ($z = 0.04$ m) and one in the oxygen sensor fitting tube ($z = 0.09$ m).

The single-bubble injection device consisted of a pressurized vessel filled with tracer gas connected with the bubble injector. The latter consisted of a 10 mm ID nozzle mounted along the column centerline and releasing gas at a distance $z_{in} = 0.01$ m above the gas distributor. Steel nets of proper mesh size were fitted inside the nozzle to prevent weeping of bed solids. The gas volume released by the pressurized vessel was preset at the desired final bubble volume, it flowed through the tube and was emitted into the bed through the nozzle forming a single bubble. The injection tube crossed the windbox and was in contact with the ceramic rings of the packing in order to preheat the bubble gas. It was continuously flushed by tracer gas in order to keep the tube clean. The reliability of the single-bubble injector was preliminarily checked in a 2-D fluidized bed operated at ambient conditions.[30] Possible leakage of gas across the bubble boundary was checked for as indicated by Solimene et al.[29] and taken into account when calculating the bubble volume.

The reactor could be operated at temperatures up to 1123 K by electrical heating. To this end, it was equipped with ceramic mat heaters driven by a PID controller based on the signal from the K-type thermocouple immersed in the bed.

Fluidizing gas was metered with a mass flow controller in the range 0.1-10 m^3/h at room-temperature.

Diagnostics

The fluidization column was equipped with four commercial oxygen solid-state sensors (custom-made type SIRO2 C700+ assembled in a DS probe) shown in Figure 1:II. The core of the sensor consists of a stabilized zirconia-based cylindrical pellet (4 mm dia., 3 mm thick) sealed at the end of a 6 mm dia. alumina tube. The sensor electrodes are made of porous platinum and coat the inner and the outer surfaces of the zirconia pellet. Air, continuously fed to the inner surface of the zirconia pellet, was used as reference gas. An R-type thermocouple is kept in contact with the inner surface of the zirconia pellet to measure the sensor tip temperature. An electromotive force (V) is generated when the two sensor tip surfaces are exposed to gases at different oxygen concentration. V is related to oxygen concentration in the test gas according to the Nernst equation[31]

$$V = -RT/nF \ln(P_{O_2}/P_{O_2}^{ref}) \tag{8}$$

where R, T, F, n, P_{O_2} and $P_{O_2}^{ref}$ are the gas constant, the sensor tip temperature, the Faraday constant, the number of electrons involved in the electrochemical reaction and the oxygen partial pressure in the test gas and in the reference gas, respectively.

Thanks to the small size of the sensor tip, the sensor re-

Table 1. Properties of Bed Material

Material	Silica sand	
Size range, μm	500–600	1180–1400
Density, kg/m^3	2600	
Group according to Geldart classification	B (α = 1.48–2)	D (α = 0.3–0.45)
Incipient fluidization velocity @ 1123K and 101 kPa, m/s		
Experimental	0.117	0.560
Theoretical[(1)]	0.138	0.488
Particle Reynolds number at incipient fluidization	0.412	4.63

[(1)]Calculated according to Wen and Yu.[32]

sponse-time to change of oxygen concentration was smaller than 10 ms.

Preliminary tests were carried out to verify the reliability and reproducibility of the sensors at the temperature of 1123 K and to calibrate them. The departure of the electromotive force V from the value V_0 measured in air was expressed as

$$V = V_0 - (RT/nF)\ln(y_{O_2}/y_{O_2}^{rif}) \quad (9)$$

Fast, high-precision piezoresistive electronic transducers were used to measure relative pressure. One of these transducers (Druck PDCR 130/C, full scale 135 mbar) measured the gas pressure inside the nozzle during single bubble injection, the others (Druck PMP 4060 full scale 70 mbar) measured gas pressure at different levels inside the bed.

Data logging was accomplished by means of a personal computer equipped with a 16 bit A/D data acquisition board (National Instruments PCI-6034E) characterized by a high sampling rate (200 kS/s). Signals from oxygen concentration and pressure transducers were sampled at the frequency of 1000 Hz for 50 s.

Materials

The fluidizing gas was technical air. High purity nitrogen was used as gas tracer.

Silica sand sieved in either the 500 – 600 μm or the 1,180 – 1,400 μm size ranges was used as bed material. Properties of the bed materials are reported in Table 1. The bed inventory was kept constant at either 1.65 or 2.2 kg corresponding to static bed heights of 0.14 and 0.19 m, respectively. These corresponded to bed aspect ratios of about 1.4 and 1.9.

Procedure

Experimental tests were carried out by injecting isolated bubbles of different diameter (D_b = 0.03, 0.04, 0.05 and 0.06 m) in incipiently fluidized beds of either bed solids with different values of the static bed height (H_{st}=0.14 and 0.19 m).

Depending on the static bed height, different configurations of oxygen sensors were arranged: for H_{st} = 0.14 m, one oxygen sensor was located inside the bed (z = 0.09 m), one at the bed surface (z = 0.14 m), one in the splash zone (z = 0.19 m) and one in the freeboard (z = 0.24 m); for H_{st} = 0.19 m, two oxygen sensors were located inside the bed (z = 0.09 and 0.14 m), one at the bed surface (z = 0.19 m), one in the splash zone (z = 0.24 m). In a few runs the radial position of the oxygen sensor tip located at z = 0.19 m, that is in the splash zone, was changed at radial positions r/r_c of 0.69, 0.49 and 0.24.

The bed was heated up to the test temperature of 1123 K while being vigorously fluidized. As thermal steadiness was approached, gas superficial velocity was decreased to the incipient fluidization velocity. Then a single bubble was suddenly injected into the bed, whose equivalent diameter was estimated by considering the volume and pressure of the vessel, and by assuming that bubble gas reached the bed temperature soon after injection. Indeed, the heat-up times of the bubble gas was estimated[33] to be smaller than 0.07 s and 0.002 s for the silica sand of 500 – 600 μm and 1,180 – 1,400 μm size ranges, respectively. The bubble volume was obtained by multiplying the injected gas volume by a factor of 0.90 – 0.92 and 0.70 – 0.50, for bed solids of 500 – 600 μm and 1,180 – 1,400 μm size, respectively, to account for gas leakage as suggested by Caram and Hsu.[34]

Data logging started just before bubble injection and lasted for 50 s.

Signals from the oxygen sensors and the pressure transducers were analyzed by means a LabVIEW® procedure to yield: the time-series of the oxygen molar fraction in the test gas and the relevant dynamical features (minimum, overshoot, rise-time) of the gas pressure and oxygen concentration signals pre-processed by a low-pass digital filter. The time-averaged axial pressure profile measured before bubble injection was worked out to estimate the actual bed voidage and height for each test with both bed materials.

Results

The matrix of experimental conditions tested included two bed solids (silica sand belonging to the 500 – 600 μm and 1,180 – 1,400 μm size ranges) and different volumes of injected bubbles. The bed materials were selected so that the finer bed solids belonged to the group B of Geldart's classification of powders, whereas the coarser belonged to group D. Correspondingly, bubbles were clouded ($\alpha = U_b\,\varepsilon_{mf}/U_{mf} \cong 1.48 - 2$) in the first case; cloudless ($\alpha \cong 0.3 - 0.45$) in the latter case.

General Phenomenology. Figure 2 shows typical results of an experiment consisting of the injection of a 0.04 m dia. nitrogen bubble in a bed of 500 – 600 μm silica sand kept at incipient fluidization by air. The static bed height was 0.19 m. The figure reports: (1) the time-series of relative pressure measured at different levels along the bed, namely z = 0.01, 0.04 and 0.09 m; (2) the time-series of oxygen mole fraction (y_{O_2}) recorded along the reactor axis at different levels, namely at z = 0.09, 0.14, 0.19 and 0.24 m. The pressure probe at z = 0.01 m was located inside the bubble injection nozzle; the others were located in the bed. Two oxygen sensors are located inside the bed (z = 0.09 m; z = 0.14 m), one at the bed surface (z = 0.19 m) and one in the splash zone (z = 0.24 m).

The pressure signal at z = 0.01 m marks the time at which a pressure perturbation associated with the bubble injection was generated in the nozzle. The origin t = 0 of the timescale was fixed at the time at which the pressure peak at z = 0.01 m was recorded.

The other two pressure probes mark the propagation of the pressure wave associated with bubble injection along the bed. Notably, the time lag between the pressure peaks at z = 0.04 m

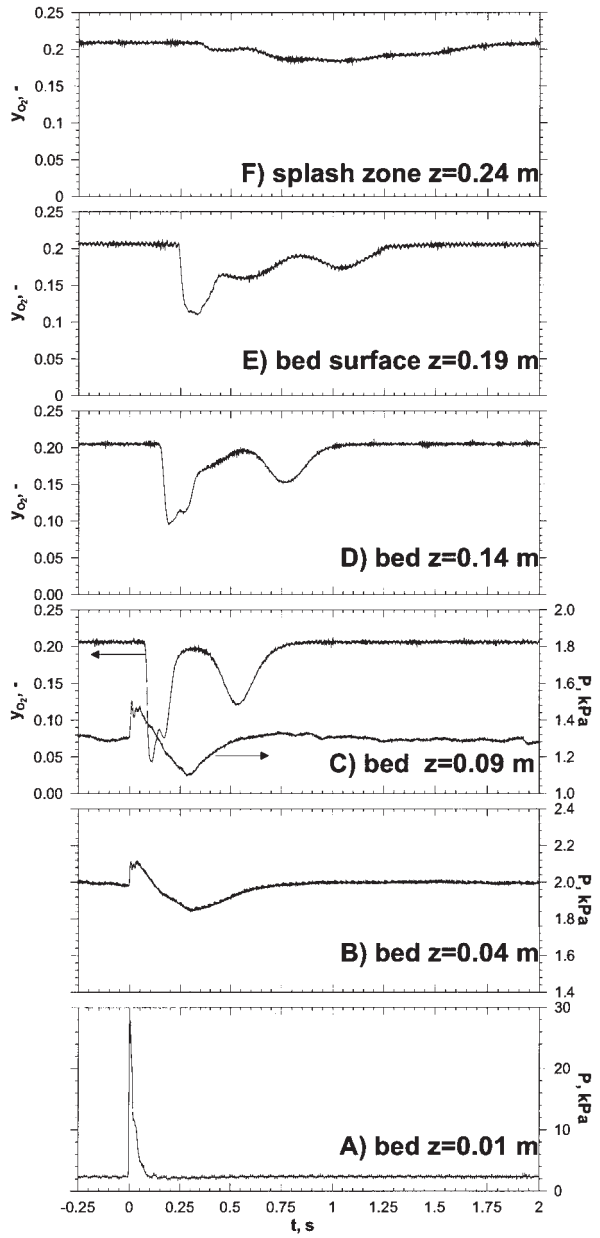

Figure 2. Oxygen molar fraction and relative gas pressure vs. time recorded at different levels along the reactor.

Operating conditions: 500 – 600 μm silica sand; H_{st} = 0.19 m; $U = U_{mf}$; T = 1,123 K; D_b =0.04 m.

and z = 0.09 m is extremely short, of the order of 5 ms, corresponding to a propagation velocity larger than 10 m/s.

The general features of the time-resolved oxygen concentration (y_{O_2}) profiles can be recognized by analyzing profiles recorded at z = 0.09 m (Figure 2C): y_{O_2} vs t profiles exhibit a characteristic bimodal feature, with a more pronounced first y_{O_2} minimum recorded 100 ms since bubble injection and a second minimum, broader and less pronounced than the first, delayed by about 500 ms with respect to the first one. On the whole, the perturbed state of the bed, represented by the departure of y_{O_2} from the baseline, lasts for about 800 ms. Closer inspection of the first peak reveals the existence of a finer dynamical structure: a second peak immediately follows the first one yielding, together with the first, a inverted saddle structure. All the reported features of the y_{O_2} vs time profiles turned out to be well reproducible as tests were repeated.

The qualitative features of oxygen concentration profiles measured at probes located at z = 0.14 and 0.19 m (Figures 2D and E) closely resemble those of profiles recorded at z = 0.09 m. Both peaks are shifted toward longer times and become broader when moving from the bottom to the top of the bed.

Oxygen concentration profile recorded in the splash zone (z = 0.24 m) differs significantly from those recorded in the bed (or at the bed surface). The departure of y_{O2} from the baseline is very limited and characterized by one minimum, very broad and not so well-defined. The initial decay of the molar fraction occurs at about 360 ms since bubble injection and the whole perturbation lasts for about 1.4 s.

The Influence of the Static Bed Height. The influence of the static bed height was investigated carrying out tests characterized by H_{st}= 0.14 m. Notably, in these tests one probe (z = 0.09 m) was located inside the bed, a second one (z = 0.14 m) was located at the bed surface, while the others (z = 0.19, and z = 0.24 m) were located at different levels in the splash zone of the bed. Oxygen concentration profiles measured inside the bed (z = 0.09 m), and at the bed surface (z = 0.14 m) are similar to those observed at the same levels with H_{st} = 0.19 m. This finding indicates that changing the static bed height has a negligible effect on y_{O_2} vs time profiles inside the bed, as well a limited influence on the profile in the splash zone, at least within the range of bubble diameters investigated. Oxygen concentration profiles recorded at the two sensors located above the bed (0.19 and 0.24 m) are similar to each other, the latter being slightly shifted and broader than the former, as a result of the combined effects of convective and dispersive phenomena that are active above the bed surface.

The Influence of the Radial Position of the Sensor Tip on Signals Recorded in the Splash Zone. A few tests were carried out to investigate how the time series of oxygen concentration recorded in the splash zone depend on the distance from the column axis, along which the trajectory of the bubble develops. Figure 3 reports oxygen concentration profiles recorded in tests where the radial position of the sensor tip located at z = 0.19 m (that is, in the splash zone) was changed taking the values r/r_c = 0.24, 0.49 and 0.69. The sensor tips at z = 0.09 m and 0.14 m (within the bed), and at 0.24 m (in the freeboard), were kept aligned along the centerline. Oxygen concentration profiles measured at 0.09, 0.14 and 0.24 m did not differ appreciably from those recorded in similar experiments with the same bubble diameter and static bed height. The oxygen concentration profile recorded in the splash zone (z = 0.19 m) depends on the radial position of the sensor tip in a nontrivial way: the perturbation induced to y_{O_2} by bubble bursting at the bed surface, represented by the departure of y_{O_2} from the baseline, is moderate at the centerline, negligible at r/r_c= 0.24 and 0.49, and maximum at r/r_c = 0.69. The bimodal character of the time-series of y_{O_2} becomes more and more evident as the sensor tip is moved away from the reactor centerline, the second minimum being far less affected by the radial position than the first one.

Influence of Bed Material. The influence of bed material was investigated by comparing results obtained with the fine

silica sand, in the size range 500 – 600 μm, with those obtained in a series of tests carried out with a bed of coarser solids, in the size range 1,180 – 1,400 μm. It must be recalled that changing bed solids corresponds to a major change of the bubbling pattern, from the fast bubble regime (finer bed material) to the slow bubble regime (coarser bed solids).

Figure 4 reports typical time-series of differential pressure (at z = 0.01, 0.04 and 0.09 m), and of oxygen molar fraction (at z = 0.09, 0.14, 0.19 and 0.24 m) measured at different levels along the bed kept at incipient fluidization. The size of the injected tracer gas bubble was D_b = 0.04 m, the static bed height was 0.19 m.

Similarly to the finer bed material, the propagation of pressure disturbances associated with bubble injection occurs at speeds much larger than 10 m/s.

Figure 5 highlights the qualitative features of oxygen concentration profiles recorded in the bed of coarse solids: a single well-defined minimum of y_{O_2} is recorded as a function of time at any bed level, shifted toward longer times when moving from the bottom to the top of the bed (Figure 4C, D and E). Notably, the profiles recorded in the splash zone and in the freeboard closely resemble those recorded within the bed.

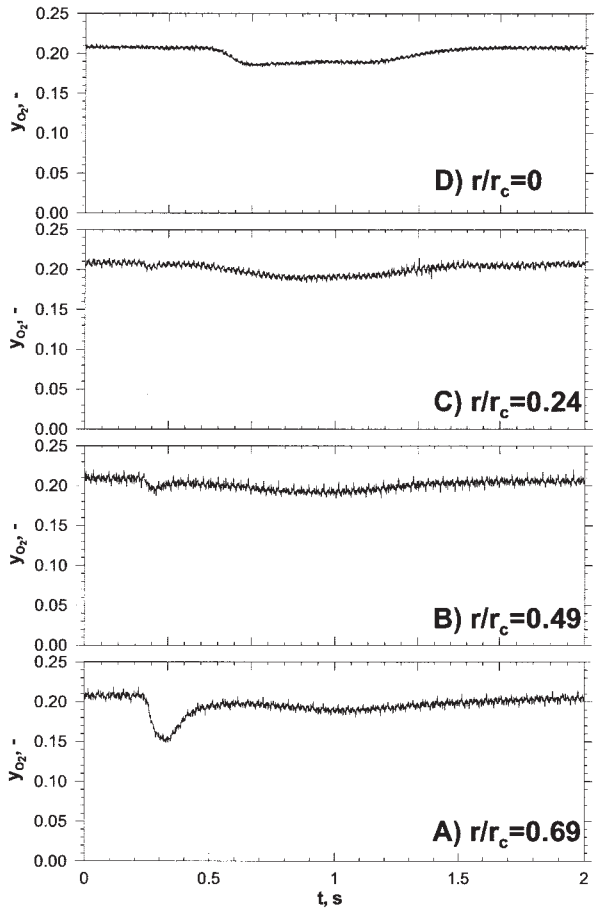

Figure 3. Oxygen molar fraction vs time recorded in the splash zone (z = 0.19 m) for runs characterized by different radial position of the probe tip (r/r_c).

Operating conditions: 500 – 600 μm silica sand; H_{st} = 0.14 m; $U = U_{mf}$; T = 1,123 K; D_b = 0.04 m.

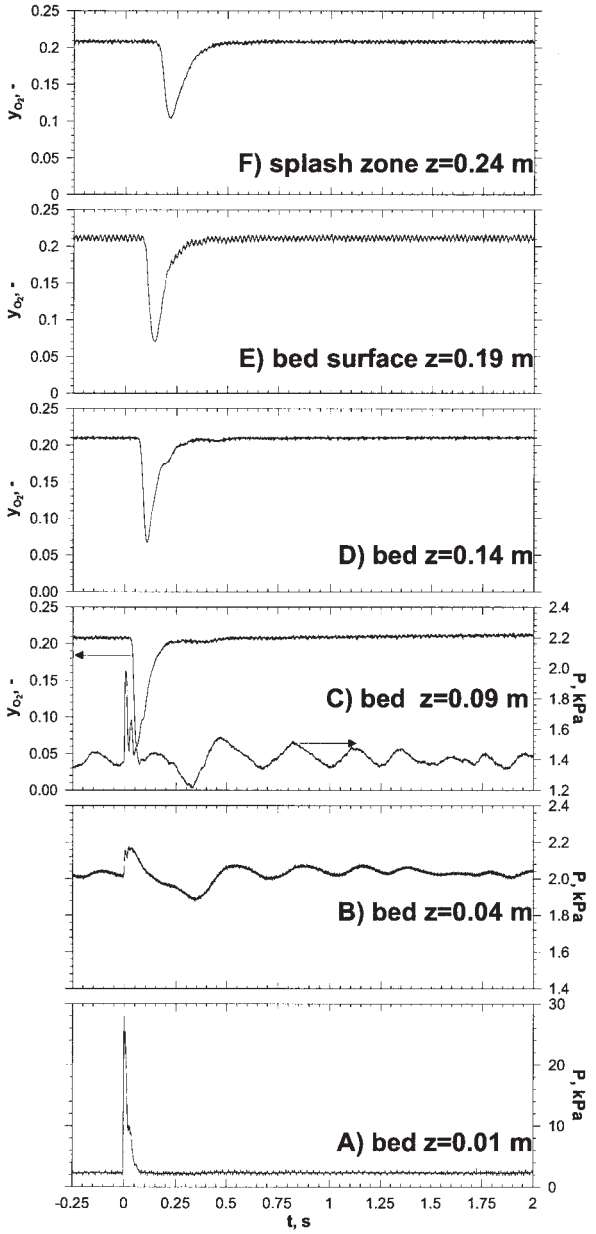

Figure 4. Oxygen molar fraction and relative gas pressure vs. time recorded at different levels along the reactor.

Operating conditions: 1,180 – 1,400 μm silica sand; H_{st} = 0.19 m; $U = U_{mf}$; T = 1,123 K; D_b = 0.04 m.

The comparison of y_{O_2} vs t profiles reported in Figure 4, with those reported in Figure 2, suggests that the bimodal character of y_{O_2} vs t profiles observed with the finer bed material is lost for the coarser material. The differences in the qualitative patterns of the time series are even more emphasized in the splash zone: the perturbation of the y_{O_2} vs t profiles with respect to the baseline is far more pronounced and confined to a much shorter time interval for the coarser bed material.

The Influence of Bubble Diameter. The influence of bubble diameter was investigated by changing the volume of tracer gas injected into the incipiently fluidized bed. Experiments were carried out with either fine or coarse bed materials. Once gas

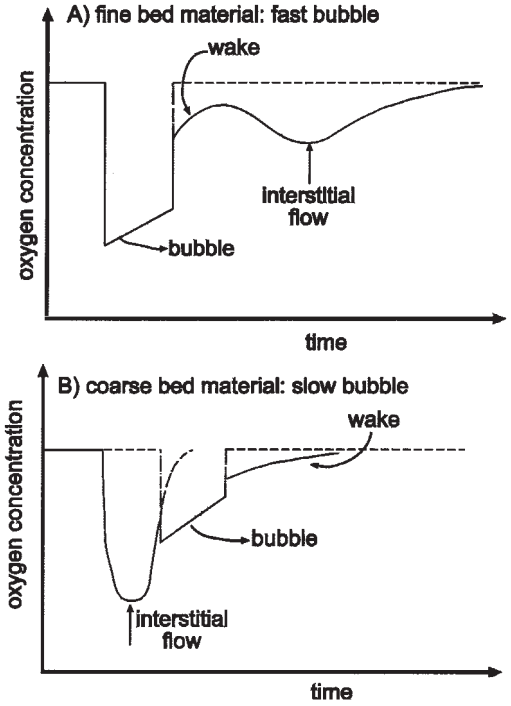

Figure 5. Conceptual framework for the interpretation of y_{O_2} vs. time profiles.

leakage from the bubble was taken into account, volumes of injected gas corresponded to bubble diameters ranging between 0.03 m and 0.06 m.

For the bed materials investigated, the qualitative features of the time-resolved oxygen concentrations measured inside the bed and at the bed surface are similar to those recorded with bubbles of 0.04 m. The minima in the y_{O_2} vs t profiles become more pronounced as D_b increases. The timing of the first y_{O_2} minimum decreases as the bubble size increases.

For the fine material, the bimodal character of the oxygen molar fraction profile recorded in the splash zone ($z = 0.24$ m, that is, 0.05 m above the bed surface) becomes more pronounced as the bubble size increases.

Discussion

The phenomenological features of pressure and oxygen concentration profiles, reported in Figures 2 through 4, can be explained by considering the combination of three processes:

- Propagation along the bed of a perturbation to the gas pressure associated with bubble injection;
- Propagation of a perturbation to the baseline oxygen concentration associated with the passage of the tracer bubble (and its wake) past the oxygen probe tip;
- Propagation of a perturbation to the baseline oxygen concentration associated with the passage of interstitial gas, enriched with tracer gas, past the probe tip.

The first process is extremely fast, as the pressure perturbation travels at a speed exceeding 10 m/s, in agreement with Musmarra et al.[35,36] It will not be taken into account in the following analysis. The features of y_{O_2} vs t profiles are explained by considering that the injection of the tracer gas bubble gives rise to the propagation of two y_{O_2} waves (Figure 5) travelling at velocities that reflect the speed of isolated bubbles, and the interstitial gas velocity, respectively. The interplay of these perturbations is critically dependent on the clouded/cloudless nature of the injected bubbles which, in turn, is dictated by bed solids size. Figure 5A provides a conceptual framework for the analysis of y_{O_2} vs t profiles observed with finer bed solids, that is, when the bubble rise velocity exceeds the interstitial gas velocity in the emulsion phase (fast bubbles). A nearly square-shaped perturbation is associated with the passage of the bubble past the probe tip, followed by a slower increase of y_{O_2} associated with the bubble wake. One further perturbation to the baseline y_{O_2} is recorded further on, related to the passage of the interstitial gas, which lags behind the bubble, past the probe tip.

A different behavior is observed in the case of coarser solids (Figure 5B). In this case the interstitial gas travels faster than the bubble (slow bubbles). The first y_{O_2} peak is related, in this case, to the passage of traced interstitial gas past the probe. Eventually, the bubble appears as a nearly square-shaped wave, followed by a tail associated with the bubble wake.

Bed Hydrodynamics. Within this framework, the analysis of the propagation of the y_{O2} minima along the bed provides a tool to assess the bubble rise velocity and the interstitial gas velocity. Figure 6 reports the timing of y_{O_2} minima recorded at different levels in response to perturbations travelling with the bubble and with the interstitial gas. Data points refer to repeated tests carried out injecting several isolated bubbles of 0.04 m dia. Both plots yield a nearly linear relationship whose slopes represent the bubble rise velocity ($U_b \cong 0.41$ m/s), and the interstitial gas velocity ($U_i \cong 0.20$ m/s), respectively. These values compare fairly well with theoretical values of 0.44 and 0.27 m/s, respectively.

Two additional features deserve mention. First, the extrapolation of the linear plot corresponding to the bubble trajectory to $t = 0$ yields $z > z_{in}$ (injection level $z_{in} = 0.01$ m). This feature should be related to the fast growth of the bubble following its nearly instantaneous injection: this would lead to an enhancement of the bubble rise velocity with respect to that

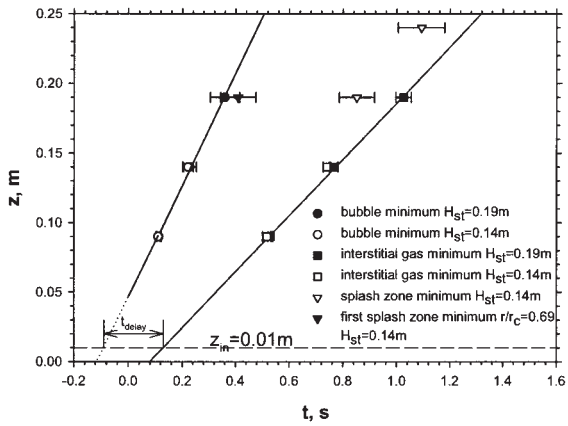

Figure 6. Timings t at which y_{O_2} minima corresponding to the bubble and to the emulsion phase are recorded at probes located at the axial coordinate z.

Dashed horizontal line marks the injection level z_{in}. Operating conditions: 500 – 600 μm silica sand; $U = U_{mf}$; $T = 1{,}123$ K; $D_b = 0.04$ m.

of a fully established isolated bubble. Second, the linear plots relative to the propagation along the bed of the two perturbations do not intersect with each other at $z = z_{in}$, as it would be expected. On the contrary, the perturbation associated with the interstitial flow lags behind the bubble by about $t_{\text{delay}} \cong 190$ ms at the bubble injection level. It can be speculated that the time lag might be related to the establishment of an interstitial gas velocity U_i smaller than U_{mf}/ε_{mf} just behind the bubble, which would delay the propagation of the perturbation associated with the interstitial flow with respect to what would be observed with a fully developed interstitial flow ($U_i = U_{mf}/\varepsilon_{mf}$). This speculation would be supported by the observation that the emulsion phase just underneath the bubble is partly defluidized and subjected to a reduced interstitial flow.[37,38]

The comparison between the measured bubble velocity and that calculated by means of the relationship

$$U_{b\infty} = 0.711\sqrt{gD_b} \tag{10}$$

is extended to different bubble diameters in Figure 7A. Similarly, the comparison between measured and theoretical values of the interstitial gas velocity is reported in Figure 7B. The relationship

$$U_i = U_{mf}/\varepsilon_{mf}(1 - k_{th}(D_b/D_c)^2) \tag{11}$$

was used for this purpose, which takes into account gas throughflow across the bubble. The throughflow increases with increasing bubble diameter and, as a consequence, the interstitial gas velocity decreases. The best agreement with experimental data was obtained by assuming a bubble throughflow velocity of about 0.64 U_{mf} ($k_{th} \cong 0.64$). The comparison between experimental and computed values of U_b and U_i is fair throughout the range of bubble diameters investigated.

Figure 7C reports the values of the initial time lag t_{delay} between the perturbations associated with the bubble and the interstitial flow as a function of bubble diameter. Values of t_{delay} are rather scattered, averaging $t_{\text{delay}} \cong 0.2$ s throughout the range of D_b investigated.

The quantitative analysis of y_{O2} vs time profiles has been extended to results obtained with coarse bed solids (1,180 – 1,400 μm), whose qualitative pattern conforms to Figure 5B. Figure 8A reports the timing at which minima of y_{O2} are recorded at different levels z in runs with 0.04 m dia.bubbles. It must be recalled that minima correspond to the perturbation travelling with the interstitial gas flow. The perturbation associated with the passage of the bubble past the probe can hardly be detected due to the following reasons: (a) the value of y_{O_2} in the bubble fast rises toward the baseline as a consequence of effective interphase mass transfer, and (b) the peak associated with the bubble largely overlaps with the tail of the perturbation due to the interstitial gas flow. Correspondingly, no data points relative to the passage of the bubble are plotted in Figure 8A.

The slope of the plot in Figure 8A yields the interstitial gas velocity U_i. Values of U_i obtained in tests with different bubble diameters are reported in Figure 8B. In this case the measured U_i is compared with values computed according to the relationship

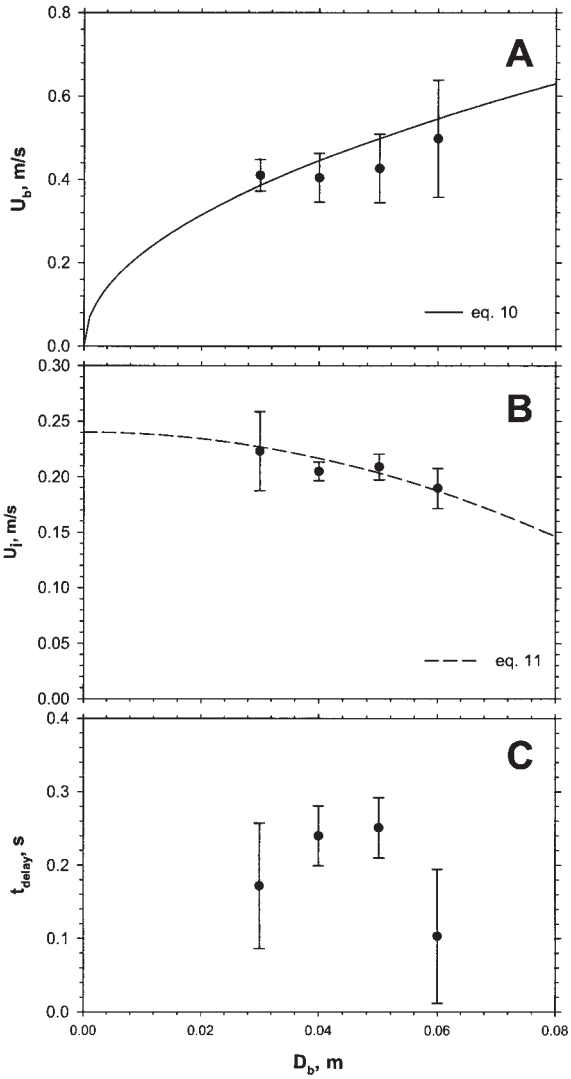

Figure 7. Hydrodynamic features of injected bubble and of the emulsion phase as a function of bubble diameter.

Operating conditions: 500 – 600 μm silica sand; H_{st} = 0.19 m; $U = U_{mf}$; T = 1,123 K. (A) bubble velocity; (B) interstitial gas velocity; (C) time delay t_{delay} between the bubble and the emulsion phase minima at $z = z_{in}$.

$$U_i = U_{mf}/\varepsilon_{mf}(1 + k_{th}(D_b/D_c)^2) \tag{12}$$

which takes into account the contribution of gas throughflow across the bubble to the interstitial gas flow. Similar to finer bed materials, gas throughflow increases with bubble diameter and, in turn, the interstitial gas velocity increases. The best fitting procedure yields a throughflow velocity of about 1.24 U_{mf} ($k_{th} \cong 1.24$).

The values of gas throughflow velocity obtained for both bed materials (ranging between $0.64 \cdot U_{mf}$ and $1.24 \cdot U_{mf}$) are in fair agreement with Murray's bubble analysis and other experimental and theoretical studies.[4,39-42]

Interphase Mass Transfer. The experimental y_{O_2} profiles were further worked out in order to calculate the overall bub-

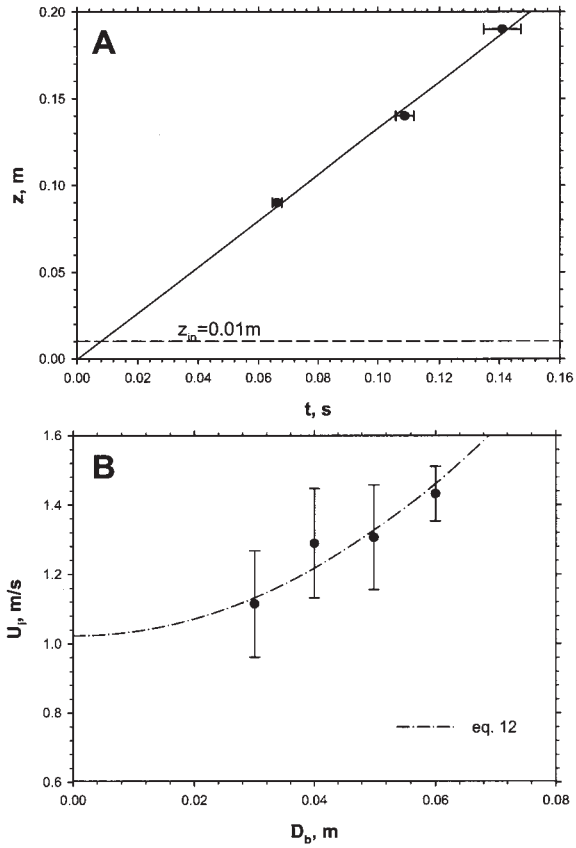

Figure 8. Hydrodynamic features of the emulsion phase as a function of bubble diameter.

Operating conditions: 1,180 – 1,400 μm silica sand; H_{st} = 0.19 m; $U = U_{mf}$; T = 1,123 K. (A) Timings t at which the y_{O_2} minimum corresponding to the emulsion phase is recorded at probes located at the axial co-ordinate z (dashed horizontal line marks the injection level z_{in}). (B) interstitial gas velocity.

ble-emulsion phase mass-transfer coefficient K_{be} according to the equation

$$\min\{y_{O_2}\} = y^0_{O_2} - (y^0_{O_2} - y^{in}_{O_2})\exp\left(-K_{be}\frac{z - z_{in}}{U_b}\right) \qquad (13)$$

where $y^0_{O_2}$ and $y^{in}_{O_2}$ are the oxygen molar fractions in air and the initial oxygen molar fraction in the bubble, respectively. Equation 13 relates the minimum value of y_{O_2} recorded at a probe, assumed equal to the value of oxygen concentration within the bubble, to the level z-z_{in} at which the probe is located relative to the bubble injection level. K_{be} was calculated from the slope of the plots of $-\ln(1 - y_{O_2}/y^0_{O_2})$ vs. z-z_{in} obtained by linearization of Eq. 13, once the value of the bubble rise velocity U_b is known.

Figure 9 refers to experiments carried out with the finer bed solids. It reports the linearized plots of $-\ln(1 - y_{O_2}/y^0_{O_2})$ vs. z-z_{in} for the various test conditions. Figure 10 compares the values of K_{be} obtained according to the above procedure with those predicted according to selected models as a function of the bubble diameter. The comparison is rather poor, the experimental data being rather insensitive to the bubble diameter, at odds with the predictions of all the theoretical relationships.

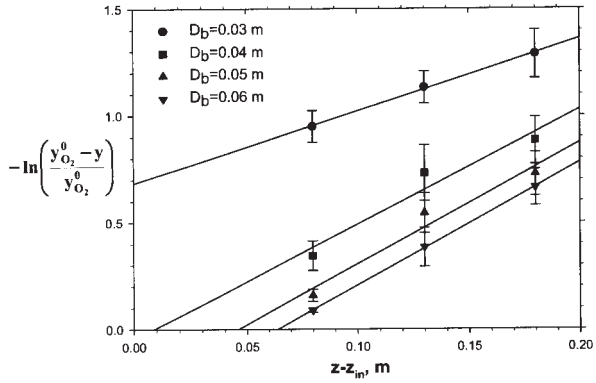

Figure 9. Linearized plot of Eq. 13.

Operating conditions: 500 – 600 μm silica sand; H_{st} = 0.19 m; $U = U_{mf}$; T = 1,123 K.

The Kunii and Levenspiel model (Eqs 2, 3 and 4), considering both the emulsion phase-cloud, and the cloud-bubble mass transfer resistances, seems to be more appropriate for the smaller bubbles. The Chiba and Kobayashi model (Eq. 5), based on the consideration of mass transfer between the cloud and the emulsion phase only, better fits experimental data for larger bubbles.

The procedure for the evaluation of K_{be} from the analysis of the linearized form of Eq. 13 could not be applied to results obtained with coarse bed solids because the value of y_{O_2} associated with the passage of the bubble could not be calculated with sufficient precision from the experimental profiles. A different method, described hereinafter, was adopted to infer the values of K_{be} from experimental data for the coarser solids.

On the basis of the conceptual framework represented in Figure 5, a model was developed with the aim of predicting the concentration of oxygen within the bubble and in the emulsion phase following the injection of an isolated bubble in an incipiently fluidized bed. The main hypotheses underlying the model are: (a) gas in the bubble is well mixed; (b) gas in the emulsion phase is in plug flow with axial dispersion, and (c)

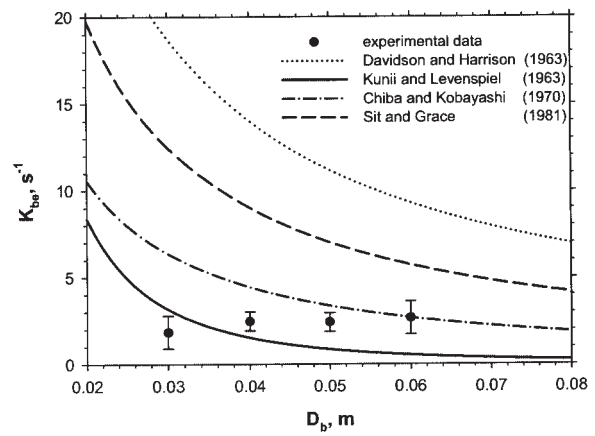

Figure 10. Overall mass-transfer coefficient between the bubble and the emulsion phase as a function of the bubble diameter.

Operating conditions: 500 – 600 μm silica sand; H_{st} = 0.19 m; $U = U_{mf}$; T = 1,123 K.

mass transfer establishes between the bubble and the neighboring emulsion phase. Model hypotheses and equations are detailed in the Appendix.

Model computations were performed with a twofold purpose:

1. for the finer solids bed, model computations aimed at checking the model's ability to reproduce the experimental y_{O_2} vs time profiles, based on the independent assessment of K_{be} as described above;

2. for the coarser solids bed, for which an independent estimate of K_{be} was not available, the model was used to infer the value of K_{be} by a best fitting procedure of the computed against experimental y_{O_2} vs time profiles.

Figure 11 provides examples of the comparison between computed and experimental y_{O_2} vs. time profiles recorded at $z = 0.14$ m. Test conditions were: $D_b = 0.04$ m; 500 – 600 μm (Figure 11A) and 1,180 – 1,400 μm (Figure 11B) bed solids; static bed height $H_{st} = 0.19$ m. For the fine solids (Figure 11A) the values of U_b, U_i and K_{be} were independently obtained as reported earlier. For the coarse solids, U_i was obtained by analysis of the experimental y_{O_2} vs time profiles (Figure 4), U_b was calculated by Eq. 10 while K_{be} was best-fitted against experimental data.

The computed profiles in Figure 11A reproduce the general features of the phenomenology, although they are inaccurate as regards the detailed structure of the y_{O_2} vs. time profiles between the two minima. This inaccuracy is essentially due to the simplified approach adopted in the model which, for instance, does not consider the existence of a bubble wake.

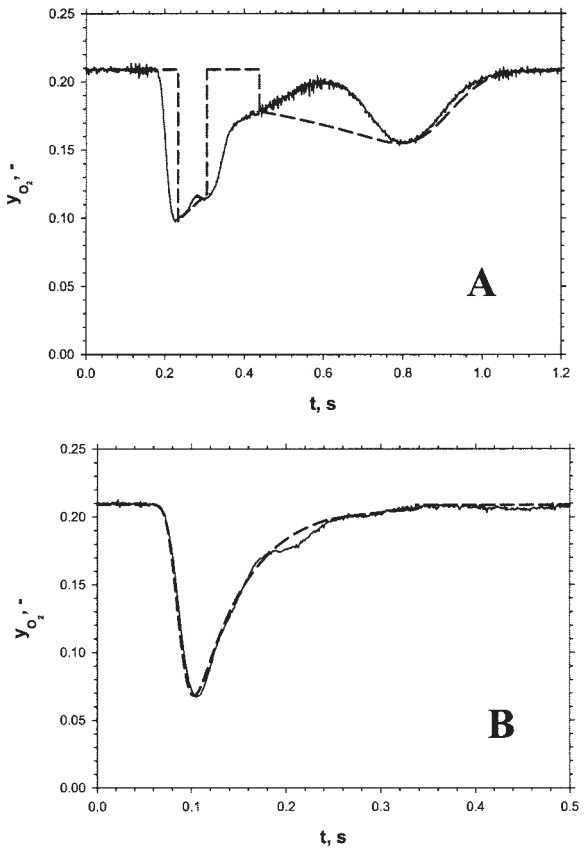

Figure 11. Experimental and computed time-resolved oxygen molar fraction.

Operating conditions: $H_{st} = 0.19$ m; $U = U_{mf}$; $T = 1{,}123$ K $D_b = 0.04$ m. Probe position: within the bed ($z = 0.14$ m). (A) bed material: silica sand 500 – 600 μm; (B) bed material: silica sand 1,180 – 1,400 μm. Solid lines: experimental profiles; Dashed lines: computed profiles.

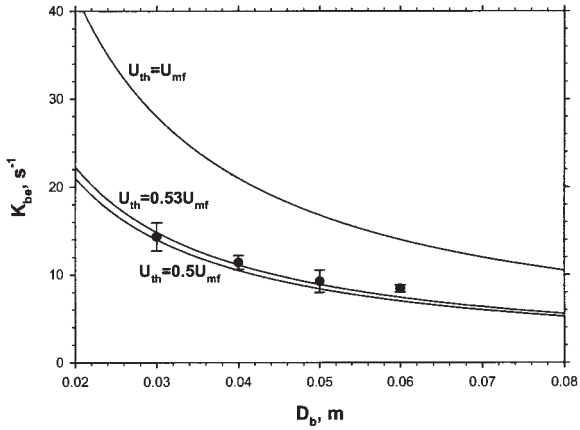

Figure 12. Overall mass-transfer coefficient between the bubble and the emulsion phase as a function of the bubble diameter.

Operating conditions: 1,180 – 1,400 μm silica sand; H_{st}= 0.19 m; $U = U_{mf}$; $T = 1{,}123$ K. Data points: experimental data; Lines: computed values according to Eq. 7 with different values of the parameter k_{th}.

For the coarser solids, the computed profiles reproduce fairly well the general features of the experimental y_{O_2} vs. time profiles, once the best-fit value of K_{be} is adopted.

Altogether, the ability of the model to reproduce the main features of the phenomenology in both cases supports the soundness of the theoretical framework that underlies the interpretation of data.

The values of K_{be} inferred for the coarse bed solids as the bubble diameter was changed between 0.03 and 0.06 m are reported in Figure 12. This figure reports, for comparison, curves obtained by applying theoretical relationships available in the literature for the prediction of K_{be} for coarse solids. Throughflow velocities ranging between $0.5 \cdot U_{mf}$ and U_{mf} were considered. It appears that experimental data points are fairly well reproduced by eq. 5 assuming a throughflow velocity of about $0.53 \cdot U_{mf}$ ($k_{th} = 0.53$).

Hydrodynamics of the Splash Zone. Analysis of y_{O_2} vs. time profiles recorded in the splash zone is now in order. Interpretation of these profiles is not straightforward, but some conclusions, mostly qualitative, can be drawn when they are interpreted in the light of the phenomenology of bubble bursting at the surface of an incipiently fluidized bed reported by Solimene et al.[29]. These authors observed, with the aid of tracer gas and a laser sheet flow visualization technique, that traced gas contained in a bubble yields, upon bursting of the bubble at the bed surface, a toroidal vortex ring located at some distance from the bubble rise trajectory.

For the finer bed solids, analysis of y_{O_2} vs time profiles recorded in the splash zone (Figs 2 and 3) indicates that:

- The y_{O_2} vs time profiles recorded at the centerline of the fluidization column display one broad minimum. Correlating the time at which the minimum y_{O_2} is observed with the timings of minima observed at probes located inside the bed (Figure 6)

it is concluded that the minimum recorded along the column centerline is the remnant of the perturbation travelling with the interstitial flow.

- The eruption of the bubble at the bed surface, on the other hand, does not significantly affect the y_{O_2} vs time profiles recorded at the column centerline ($r = 0$), that is, along the bubble rise trajectory. On the contrary, bubble bursting markedly affects the y_{O_2} vs time profiles recorded at some distance from the centerline ($r/r_c = 0.69$) (Figure 3) determining a pronounced minimum soon after bubble injection. Comparing the timing at which this minimum is observed with the timings of the bubble minimum inside the bed (Figure 6), it can be concluded that the minimum recorded at $r/r_c = 0.69$ is the remnant of the perturbation travelling with the bubble.

These findings are fully consistent with those reported by Solimene et al.[29] In particular the following features receive confirmation:

- a toroidal flow structure is established after bubble bursting, constrained by the column wall. This is consistent with the finding that wall effects are significant as the bubble-to-column diameter ratio exceeds 0.285 (it is $D_b/D_c=0.4$ in this case);
- the toroidal structure rises at a speed which lays between the bubble and the interstitial gas velocities (Figure 6).

The features of the y_{O_2} vs. time profiles recorded in the splash zone of a bed of coarser solids are rather different from those observed with the finer bed solids, reflecting the different way the perturbations develop within the bed (Figures 4 and 8). The main perturbation recorded by the probe located in the splash zone reflects that travelling in the bed with the interstitial flow. The burst of the bubble, lagging behind the first perturbation, is hardly detected at the splash zone level as the tracer gas is almost entirely transferred to the emulsion phase before the bubble arrives at the bed surface.

The appearance of a perturbation to the y_{O_2} base level at some radial distance from the column axis, and the simultaneous lack of any detectable perturbation at the probe located at the axis, support the thesis that a toroidal traced gas pocket is established in the splash zone immediately after bubble eruption. This is consistent with the phenomenological framework provided by Solimene et al.[29] It is likely that the same process takes place in experiments with coarse bed solids, not detected because, as already pointed out, most of the tracer gas leaves the bubble well before it bursts at the bed surface.

Conclusions

A novel technique has been presented for the quantitative assessment of gas mixing and hydrodynamic patterns associated with the rise of an isolated bubble in gas-fluidized beds. The technique is based on the use of an array of zirconium oxide oxygen sensors located along the axis of a fluidized-bed reactor. Tests consisted of the injection of isolated nitrogen bubbles in a hot (1,123 K) bed incipiently fluidized by air, followed by the recording of time-resolved oxygen concentration and gas pressure profiles. Two bed materials, belonging to the group B and D of the Geldart classification of powders, were tested.

Time series of oxygen concentration recorded at different levels in the bed and above the bed surface can be interpreted in the light of a conceptual framework that considers bubble motion and interstitial flow coupled with each other through mass transfer between the bubble and the emulsion phase. Quantitative analysis of the time series of oxygen concentration was accomplished with the aid of a purposely developed model and with slight modifications that depended on whether the slow or fast bubble regimes were considered. The bubble rise velocity, the velocity of the interstitial gas and the bubble-emulsion phase mass-transfer coefficient were determined and compared with predictions of theoretical relationships.

For the group B bed material, corresponding to the fast bubble regime, both the bubble rise velocity and the interstitial gas velocity determined from experimental data were fairly well predicted by the available correlations. A remarkable feature was represented by the time delay with which the interstitial flow apparently responds to the stimulus represented by the bubble injection, a feature that is speculatively related to the possible onset of partial defluidization of the emulsion phase underneath the bubble. Bubble-emulsion phase mass transfer coefficients range between 2 and 3 s^{-1}, characterized by a very limited dependence on bubble size, at odds with the predictions of available correlations. Quantitative agreement is better with the Kunii and Levenspiel[11] equation for smaller bubble diameters, with the Chiba and Kobayashi[13] equation for larger bubbles. Analysis of oxygen concentration time series recorded in the splash zone supports the view that a traced bubble yields upon bursting a toroidal pocket of tracer gas at some distance from the original bubble trajectory.

For the group D material, bubble-emulsion phase mass transfer was far more effective than that observed with the group B material. This made the detection of the passage of the bubble past the sensors more difficult or even impossible. Measured interstitial gas velocities were fairly well predicted by correlations also in this case. The bubble-emulsion phase mass transfer coefficient was in the range 18 to 10 s^{-1} as the bubble diameter varied between 0.03 and 0.06 m. Theoretical relationships for the prediction of the bubble-emulsion phase mass-transfer coefficient, based on the hypothesis that gas throughflow velocity is 0.53 times the incipient fluidization velocity reproduce with good accuracy the experimental data.

Acknowledgments

The assistance of Mr. Antonio Cammarota in the set up of the experimental apparatus and of Mr. Antonio Telesca in the experimental campaign and in the setup of the model are gratefully acknowledged.

Notation

C_{Ab} = concentration of compound A in the bubble, mol/m^3
C_{Ae} = concentration of compound A in the emulsion phase, mol/m^3
D = molecular-diffusion coefficient, m^2/s
D_a = dispersion coefficient, m^2/s
D_b = bubble diameter, m
D_c = column diameter, m
F = Faraday constant, C/mol
f_w = volumetric fraction of bubble wake, m^3/m^3
g = acceleration due to gravity, m/s^2
H_{st} = static bed height, m
k = constant in Eq. A4
k_{th} = throughflow constant
K_{bc} = mass-transfer coefficient between the bubble and the cloud, s^{-1}
K_{be} = overall mass-transfer coefficient between the bubble and the emulsion phase, s^{-1}
K_{ce} = overall mass-transfer coefficient between the cloud and the emulsion phase, s^{-1}
n = number of electrons involved in the electrochemical reactions

N_{Ab} = moles of compound A in the bubble, mol
P = relative gas pressure, Pa
P_{O_2} = oxygen partial pressure in the test gas, Pa
$P_{O_2}^{ref}$ = oxygen partial pressure in the test gas, Pa
Q_f = volumetric flow rate in the buffer zone, m^3/s
r = radial co-ordinate, m
r_c = column radius, m
R = gas constant, J/molK
s = variable in Laplace-domain
S = cross-sectional area section of the buffer zone, m^2
t = time, s
t_d = time lag in Eq. A16, s
t_{delay} = initial time delay between the bubble and the interstitial flow, s
T = temperature, K
u = Heaviside function
U = fluidization velocity, m/s
U_b = bubble velocity, m/s
$U_{b\infty}$ = bubble velocity according to Eq. 10, m/s
U_i = interstitial gas velocity, m/s
U_{mf} = incipient fluidization gas velocity, m/s
V = electromotive force, V
V_O = electromotive force in air, V
V_b = bubble volume, m^3
y_{O_2} = oxygen molar fraction, -
$y_{O_2}^{ein}$ = oxygen molar fraction in the input of buffer zone
$y_{O_2}^{eout}$ = oxygen molar fraction in the output of buffer zone
$y_{o_2}^{in}$ = initial oxygen molar fraction in the bubble
$y_{o_2}^{0}$ = oxygen molar fraction in air
z = axial co-ordinate, m
z_i = level of the output of buffer zone, m
z_{in} = level of the bubble injection, m

Greek symbols

α = ratio between bubble velocity and interstitial fluidizing gas velocity
ε_{mf} = bed voidage at incipient fluidization

Superscripts

* = dimensionless variable
e = emulsion phase
b = bubble

Literature Cited

1. Stephens GK, Sinclair RJ, Potter OE. Gas exchange between bubbles and dense phase in a fluidized bed. *Powder Technol*. 1967;1:157-166.
2. Drinkenburg AAH, Rietema K. Gas transfer from bubbles in a fluidized bed to the dense phase-I. Theory. *Chem Eng Sci*. 1972;27:1765-1774.
3. Drinkenburg AAH, Rietema K. Gas transfer from bubbles in a fluidized bed to the dense phase-II. Experiments. *Chem Eng Sci*. 1973;28: 259-273.
4. Walker BV. The effective rate of gas exchange in a bubbling fluidized bed. *Trans of the Inst of Chem Eng*. 1975;53:255-266.
5. Werther J. Hydrodynamics and mass transfer between the bubble and emulsion phases in fluidized beds of sand and cracking catalyst. In Kunii D, Cole SS. Eds. *The Proceedings of the 4th International Conference on Fluidization*. New York: Engineering Foundation; 1984:93-101.
6. Qin J, Wang Z. Gas exchange between bubble and emulsion phases in bubbling fluidized beds. In: Kwauk M, Kunii D, Jiansheng Z, Hasatani M (Eds), *Fluidization '85 Science and Technology, the Proceedings of the 2nd China-Japan Symposium on Fluidization*. New York: Elsevier Science Pub. Co; 1985:274-282.
7. Kai T, Imamura T, Takahashi T. Hydrodynamic influences on mass transfer between bubble and emulsion phases in a fine particle fluidized bed. *Powder Technol*. 1995;83:105-110.
8. Schlichthaerle P, Hartge E-U, Werther J. Interphase mass transfer and gas mixing in the bottom zone of a circulating fluidized bed. In: Kwauk M, Li J, Yang W-C (Eds), *Fluidization X, The Proceedings of the 10th International Conference on Fluidization*. New York: Engineering Foundation; 2001:549-556.
9. Wu W, Agarwal PK. The effect of bed temperature on mass transfer between the bubble and emulsion phases in a fluidized bed. *The C J of Chem Eng*. 2003;81:940-948.
10. Davidson JF, Harrison D. *Fluidised Particles*. New York: Cambridge Press; 1963.
11. Kunii D, Levenspiel O. Bubbling bed model - Model for the flow of gas through a fluidized bed. *Ind & Eng Chem*. 1968;7:446-452.
12. Higbie R. The rate of absorption of a pure gas into a still liquid during short periods of exposure. *Transactions of the American Institute of Chemical Engineers*. 1935;31:365-389.
13. Chiba T, Kobayashi H. Gas exchange between the bubbles and emulsion phases in gas-solid fluidized beds. *Chem Eng Sci*. 1970;25:1375-1385.
14. Murray JD. On the mathematics of fluidization - Part 2. Steady notion of fully developed bubbles. *J of Fluid Mechanics*. 1965;22:57-80.
15. Sit SP, Grace JR. Effect of bubble interaction on interphase mass transfer in gas fluidized beds. *Chem Eng Sci*. 1981;36:327-335.
16. Chavarie C, Grace JR. Interphase mass transfer in a gas-fluidized bed. *Chem Eng Sci*. 1976;31:741-749.
17. Sit SP, Grace JR. Interphase mass transfer in an aggregative fluidized bed. *Chem Eng Sci*. 1978;33:1115-1122.
18. Lignola PG, Donsì G, Massimilla L. Mass spectrometric measurements of gas composition profiles associated with bubbles in a two dimensional bed. *AIChE Symposium Series*. 1983;79:19-26.
19. Naruse I, Kuramoto K, Ohtake K. Influence of bubble and emulsion phase on N2O formation in bubbling fluidized bed coal combustion by conditional sampling. In: Large JF, Laguerie C. (Eds) *Fluidization VIII, The Proceedings of the 8th International Conference on Fluidization*. New York: Engineering Foundation; 1995:113-120.
20. Turnbull E, Davidson JF. Fluidized combustion of char and volatiles from coal. *AIChE J*. 1984;30:881-889.
21. Van der Honing G. Volatile and char combustion in large scale fluidized bed coal combustors. Ph.D. Thesis. The Netherlands: University of Twente; 1991.
22. Scala F, Salatino P. Modeling fluidized bed combustion of high-volatile solid fuels. *Chem Eng Sci*. 2002;57:1175-1196.
23. Pemberton ST, Davidson JF. Turbulence in the freeboard of a gas-fluidised bed. *Chem Eng Sci*. 1984;39:829-840.
24. Zenz FA, Weil NA. A theoretical-empirical approach to the mechanism of particle entrainment from fluidized beds. *AIChE J*. 1958;4: 472-479.
25. Horio M, Taki A, Hsieh, YS, Muchi I. Elutriation and particle transport through the freeboard of a gas-solid fluidized bed. In: Grace RJ, Matsen M. (Eds), *Fluidization, The Proceedings of the 3th International Conference on Fluidization*. New York: Plenum Press; 1980: 509-518.
26. Levy Y, Lockwood FC. Laser doppler measurements of flow in freeboard of a fluidized bed. *AIChE J*. 1983;29:889-895.
27. Caram HS, Efes Z, Levy EK, Gas and particle motion induced by a bubble eruption at the surface of a gas fluidized bed. *AIChE Symposium Series*. 1984;80(234):106-113.
28. Yorquez-Ramirez MI, Duursma GR, Study of the flow pattern above an erupting bubble in an incipiently fluidised bed using image shifting. *Chem Eng Sci*. 2000;55:2055-2064.
29. Solimene R, Marzocchella A, Ragucci R, Salatino P. Flow structures and gas-mixing induced by bubble bursting at the surface of an incipiently gas-fluidized bed. *Ind & Eng Chem Res*. 2004;43:5738-5753.
30. Solimene R. Fenomeni di segregazione di fasi gassose e di particelle combustibili nella combustione di solidi in letto fluidizzato. PhD Thesis. Napoli: Università degli Studi di Napoli Federico II; 2003.
31. Moseley PT, Norris J, Williams, DE. *Techniques and mechanisms in gas sensing*. Bristol: Adam Hilger; 1991.
32. Wen CY, Yu YH. A generalized method for predicting the minimum fluidization velocity. *AIChE J*. 1966;12:610-612.
33. Wu W, Agarwal PK. Heat transfer to an isolated bubble rising in a high-temperature incipiently fluidized bed. *The C J of Chem Eng*. 2004;82:399-405.
34. Caram HS, Hsu K-K. Bubble formation and gas leakage in fluidized beds. *Chem Eng Sci*. 1986;41:1445-1453.
35. Musmarra D, Vaccaro S, Filla M, Massimilla L. Propagation characteristics of pressure disturbances originated by gas jets in fluidized beds. *Int J of Multiphase Flow*. 1992;18:965-976.

36. Musmarra D, Poletto M, Vaccaro S, Clift R. Dynamic waves in fluidized beds. *Powder Technol.* 1995;82:255-268.
37. Horio M, Iwadate Y, Sugaya T. Particle normal stress distribution around a rising bubble in a fluidized bed. *Powder Technol*. 1998;96: 148-157.-
38. Campbell CS. Granular flows and gas-fluidization. In: Arena U, Chirone R, Miccio M, Salatino P (Eds), *Fluidization XI - Present and future for fluidization engineering, the Proceedings of the 11th International Conference on Fluidization*. New York: Engineering Foundation; 2004:21-35.
39. Partridge BA, Rowe PN. Analysis of gas flow in a bubbling fluidized bed when cloud formation occurs. *Trans of the Inst of Chem Eng*. 1966;44:349-358.
40. Hailu L, Plaka F, Clift R, Davidson JF. Measurement of gas flow through a two-dimensional bubble in a fluidised bed. *Chem Eng Res and Design.* 1993;71:382-389.
41. Gautam M, Jurewicz JT, Kale SR. An experimental investigation of throughflow velocities in two-dimensional fluidized bed bubbles: laser Doppler anemometer measurements. *J of Fluids Eng*. 1994;116:605-612.
42. Gera D, Gautam M. Analysis of throughflow velocity in two-dimensional fluidized bed bubbles. *J of Fluids Eng*. 1995;117:319-322.
43. Levenspiel O. *Chemical Reaction Engineering.* 3rd ed. New York: John Wiley & Sons, Inc; 1999.

Appendix: The simulation model

Model assumptions

The model aims at the prediction of the time series of oxygen molar fraction at specified positions along the bed axis after the injection of a nitrogen bubble in a bed kept at incipient fluidization by a stream of air. Only two species are present in the bed, namely nitrogen and oxygen. Bubble motion, bubble-emulsion phase mass transfer and interstitial flow in the emulsion phase are considered, which combine with each other to give rise to two perturbations in the oxygen molar fraction field, one associated with the bubble, the other with the interstitial flow. The model is based on the set up of mass balance equations on oxygen referred to the bubble and the interstitial gas and is based on the following assumptions:

1. The spatial domain is divided into three zones:(a) the bubble, (b) a "buffer" zone within the emulsion phase surrounding the bubble and moving with it, and (c) the remainder of the emulsion phase. The buffer zone is a cylinder whose diameter is proportional to the bubble diameter and whose height equals the bubble diameter.
2. The bubble is well mixed.
3. Gas in the emulsion phase is in plug flow with axial dispersion. The axial dispersion coefficient D_a ranged between 0.001 and 0.0001 m^2/s depending on bed solids size.[43]
4. Mass transfer phenomena between the bubble and the emulsion phase involves only the buffer zone. The driving force to mass transfer is given by the difference between oxygen concentration at the inlet of the buffer zone and that in the bubble.
5. Radial dispersion in the gas phase is neglected.
6. Oxygen concentration at the inlet of the buffer zone equals oxygen concentration in air.

For computational convenience, model equations are set up in a Lagrangian one-dimensional spatial frame of reference moving with the bubble and whose origin is at the bubble nose. In this frame of reference the emulsion phase moves upward in the case of *slow* bubbles ($U_b < U_{mf}/\varepsilon_{mf}$), downward in the case of *fast* bubbles ($U_b > U_{mf}/\varepsilon_{mf}$).

The choices made in setting up the model are such that model equations relative to the bubble and the emulsion phase can be solved in a sequential manner.

Model equations

Mass Balance on the Bubble. The mass balance on oxygen yields

$$\frac{dy^b_{O_2}}{dt} = K_{be}(y^{ein}_{O_2} - y^b_{O_2}) \tag{A1}$$

with the initial condition:

$$t = 0 \quad y^b_{O_2} = 0$$

where $y^b_{O_2}$ $y^{ein}_{O_2}$ are, respectively, the oxygen molar fraction in the bubble and, according to assumption 4, the oxygen molar fraction at the inlet of the buffer zone.

Material Balance on the Buffer Zone. The mass balance on oxygen in the buffer zone reads

$$Q_f(y^{ein}_{O_2} - y^{eout}_{O_2}) + K_{be}V_b(y^b_{O_2} - y^{ein}_{O_2}) = 0 \tag{A2}$$

where $y^{eout}_{o_2}$ is the oxygen molar fraction in the stream issuing from the buffer zone. The volumetric flow rate Q_f flowing across the buffer zone is given by:

$$Q_f = (U_i - U_b)\varepsilon_{mf}S \tag{A3}$$

where the cross-sectional area of the buffer zone is:

$$S = \frac{(kD_b)^2}{4} \tag{A4}$$

taking values of $k \cong 1$.

Material Balance on the Emulsion Phase. The mass balance on oxygen in the emulsion phase, considering assumption 3, yields

$$\frac{\partial y^e_{O_2}}{\partial t} + (U_i - U_b)\frac{\partial y^e_{O_2}}{\partial z} = D_a\frac{\partial^2 y^e_{O_2}}{\partial z^2} \tag{A5}$$

$$\begin{array}{lll} \text{I.C.:} & t = 0 & y^e_{O_2} = y^0_{O_2} \\ \text{B.C.:} & z = z_i & y^e_{O_2} = y^{eout}_{O_2} \\ & z \to +\infty & y^e_{O_2} = y^0_{O_2} \end{array}$$

where z_i is the level of the surface corresponding to the output of the buffer zone.

Solution procedure

According to assumption 5:

$$y^{ein}_{O_2} = y^0_{O_2} \tag{A6}$$

and assuming

$$y^*_{O_2} = \frac{y^0_{O_2} - y_{O_2}}{y^0_{O_2}} \tag{A7}$$

Eqs A1, A2 and A5 become

$$\frac{d y^{*\,b}_{O_2}}{dt} = -K_{be} y^{*b} \tag{A8}$$
$$t = 0 \quad y^{*\,b}_{O_2} = 1$$

$$y^{*\,e\text{out}}_{O_2} = \frac{K_{be} V_b}{Q_f} y^{*\,b}_{O_2} \tag{A9}$$

$$\frac{\partial y^{*\,e}_{O_2}}{\partial t} + (U_i - U_b)\frac{\partial y^{*\,e}_{O_2}}{\partial z} = D_a \frac{\partial^2 y^{*\,e}_{O_2}}{\partial z^2} \tag{A10}$$
$$t = 0 \qquad y^{*\,e}_{O_2} = 0$$
$$z = z_i \qquad y^{*\,e}_{O_2} = y^{*\,e\text{out}}_{O_2}$$
$$z \to +\infty \quad y^{*\,e}_{O_2} = 0$$

Equation A8 yields

$$y^{*\,b}_{O_2} = e^{-K_{be} t} \tag{A11}$$

Substituting Eq. A11 in Eq. A9 yields

$$y^{*\,e\text{out}}_{O_2} = \frac{K_{be} V_b}{Q_f} e^{-t K_{be}} \tag{A12}$$

The partial-differential Eq.A10 is Laplace-transformed

$$s y^{*\,e}_{O_2} + (U_i - U_b)\frac{\partial y^{*\,e}_{O_2}}{\partial z} = D_a \frac{\partial^2 y^{*\,e}_{O_2}}{\partial z^2} \tag{A13}$$
$$z = z_i \qquad y^{*\,e}_{O_2} = \frac{K_{be} V_b}{Q_f}\frac{1}{s + K_{be}}$$
$$z \to +\infty \quad y^{*\,e}_{O_2} = 0$$

The second-order ODE Eq. A13 is solved analytically

$$y^{*\,e}_{O_2} = \frac{K_{be} V_b}{Q_f}\frac{1}{s + K_{be}} e^{(((U_b - U_i)/2D_a) - (1/2)\sqrt{((U_b - U_i)/D_a)^2 + (4s/D_a)})(z - z_i)} \tag{A14}$$

The solution Eq. A14 in the Laplace domain yields, by inverse transformation, the oxygen molar fraction $y^{*\,e}_{O_2}$ in the time domain as a function of the axial co-ordinate z

$$y^{*\,e}_{O_2} = \frac{K_{be} V_b}{Q_f} e^{-((U_b - U_i)/2D_a)(z - z_i)} \int_0^t e^{-K_{be}\tau} \frac{z - z_i}{2\sqrt{\pi D_a (t - \tau)^3}} e^{-((t-\tau)/4D_a)((U_b - U_i)^2 + ((z - z_i)/(t - \tau))^2)} d\tau \tag{A15}$$

Equation A15 is independent on whether the slow or fast bubble regime applies. The solution in a Eulerian reference frame is obtained by applying the following co-ordinate transformation to evaluate the position of the output surface of the buffer zone z_i:

- slow bubbles: $z_i = U_b t$;
- fast bubbles: $z_i = U_b t - D_b$.

The oxygen molar fraction vs time recorded inside the fluidized bed at z is given, in an Eulerian frame of reference, by

slow bubbles $y_{O_2}(t)$

$$= y^0_{O_2}\left((1 - y^{*\,e}_{O_2}(t))\left(1 - u\left(t - \frac{z}{U_b}\right)\right) + \left(1 - y^{*\,b}_{O_2}(t)\left(u\left(t - \frac{z}{U_b}\right) - u\left(t - \frac{z + D_b}{U_b}\right)\right)\right)\right)$$

fast bubbles $y_{O_2}(t)$

$$= y^0_{O_2}\left((1 - y^{*\,e}_{O_2}(t - t_d))u\left(t - \left(\frac{z + D_b}{U_b} + t_d\right)\right) + \left(1 - y^{*\,b}_{O_2}(t)\left(u\left(t - \frac{z}{U_b}\right) - u\left(t - \frac{z + D_b}{U_b}\right)\right)\right)\right) \tag{A16}$$

where u is the Heaviside function and $t_d = t_{\text{delay}} - (D_b/U_b)$ represents the time lag between signals travelling with the emulsion phase and the bubble in the fast bubbles regime.

Manuscript received Jan. 19, 2005, and revision received Apr. 28, 2005.